

## A STARBURSTING PROTO-CLUSTER IN MAKING ASSOCIATED WITH A RADIO GALAXY AT $z = 2.53$ DISCOVERED BY $H\alpha$ IMAGING

MASAO HAYASHI<sup>1</sup>, TADAYUKI KODAMA<sup>1,2</sup>, KEN-ICHI TADAKI<sup>1,3</sup>, YUSEI KOYAMA<sup>1,4</sup>, AND ICHI TANAKA<sup>2</sup>

<sup>1</sup> Optical and Infrared Astronomy Division, National Astronomical Observatory, Mitaka, Tokyo 181-8588, Japan; masao.hayashi@nao.ac.jp

<sup>2</sup> Subaru Telescope, National Astronomical Observatory of Japan, 650 North A'ohoku Place, Hilo, HI 96720, USA

<sup>3</sup> Department of Astronomy, Graduate School of Science, University of Tokyo, Tokyo 113-0033, Japan

<sup>4</sup> Department of Physics, Durham University, South Road, Durham, DH1 3LE, UK

Received 2012 April 13; accepted 2012 July 19; published 2012 August 30

### ABSTRACT

We report a discovery of a proto-cluster in vigorous assembly and hosting strong star-forming activities, associated with a radio galaxy USS 1558-003 at  $z = 2.53$ , as traced by wide-field narrow-band  $H\alpha$  imaging with MOIRCS on the Subaru Telescope. We find 68  $H\alpha$  emitters with dust-uncorrected star formation rates (SFRs) down to  $8.6 M_{\odot} \text{ yr}^{-1}$ . Their spatial distribution indicates that there are three prominent clumps of  $H\alpha$  emitters: one surrounding the radio galaxy, the second located at  $\sim 1.5$  Mpc away to the southwest, and the third located between the two. These contiguous three systems are very likely to merge together in the near future and may grow to a single more massive cluster at a later time. While most  $H\alpha$  emitters reside in the “blue cloud” on the color–magnitude diagram, some emitters have very red colors with  $J - K_s > 1.38(\text{AB})$ . Interestingly, such red  $H\alpha$  emitters are located toward the faint end of the red sequence, and they tend to be located in high density clumps. We do not see any statistically significant difference in the distributions of individual SFRs or stellar masses of the  $H\alpha$  emitters between the dense clumps and the other regions, suggesting that this is one of the notable sites where the progenitors of massive galaxies in the present-day clusters were in their vigorous formation phase. Finally, we find that  $H\alpha$  emission of the radio galaxy is fairly extended spatially over  $\sim 4''$ . However, it is not as widespread as its  $\text{Ly}\alpha$  halo, meaning that the  $\text{Ly}\alpha$  emission is indeed severely extended by resonant scattering.

*Key words:* galaxies: clusters: general – galaxies: clusters: individual (USS 1558-003) – galaxies: evolution

*Online-only material:* color figures

### 1. INTRODUCTION

It is well known that galaxy properties are strongly dependent on the environments in which galaxies reside (e.g., Dressler et al. 1997; Tanaka et al. 2005; Cucciati et al. 2006). Galaxy clusters are one of the most biased environments in the universe, and local ones are dominated by galaxies with red colors and elliptical morphologies that have already quenched their star-forming activities and are passively evolving. In contrast, star-forming galaxies with a blue color and spiral/irregular morphologies are preferentially found in the field environment. This trend is known as a star formation–density relation where star formation activity of galaxies decreases gradually in higher density regions (e.g., Kauffmann et al. 2004; Cooper et al. 2008). It is certain that some processes specific to the high density environment play an important role in the formation and evolution of elliptical galaxies found in the local universe. The plausible environmental effects include galaxy–intracluster medium interactions such as ram-pressure stripping (Gunn & Gott 1972), galaxy–cluster gravitational interactions (Byrd & Valtonen 1990), and galaxy–galaxy interactions such as mergers and harassment (Moore et al. 1996). However, the relative importance of the processes still remains unclear.

The fraction of blue star-forming galaxies in galaxy clusters increases with redshifts up to  $z \sim 1$  (Butcher–Oemler effect, Butcher & Oemler 1978, 1984). Recent observations have revealed that there are many starburst galaxies even in high density regions at  $z \gtrsim 1.5$  (Hayashi et al. 2010; Hilton et al. 2010; Papovich et al. 2010; Tran et al. 2010; Fassbender et al. 2011). However, as their color–magnitude diagrams show a prominent red sequence, a large fraction of passive galaxies

also exist in these clusters; thus, the formation epoch of such massive galaxies seems to be much earlier. Indeed, Gobat et al. (2011) have found that there are already mature galaxies in a cluster at  $z = 2.07$ , which is the most distant X-ray cluster to date. It is essential to survey dense regions at higher redshifts of  $z \gtrsim 2$  in more detail to investigate the site where a large fraction of progenitors of local elliptical galaxies are evolving vigorously and reveal critical processes for their evolution, although these recent studies obviously suggest that star-forming activity of galaxies becomes more active with increasing redshifts. The importance of surveys in high density regions at  $z \gtrsim 2$  is supported by the fact that the activities of galaxies and active galactic nuclei (AGNs) have peaks at  $z = 1\text{--}3$  (i.e., Madau et al. 1996; Hopkins & Beacom 2006; Ueda et al. 2003). Moreover, it should be noted that massive galaxies on the red sequence disappear in proto-clusters at  $z \sim 3$  (Kodama et al. 2007), while such red galaxies are already in place in proto-clusters at  $z \sim 2$  (see also Kajisawa et al. 2006a; Kriek et al. 2008; Doherty et al. 2010).

Proto-clusters at  $z \gtrsim 2$  are ideal targets for investigating the environmental dependence of galaxy properties at high redshift. High- $z$  radio galaxies (HzRGs) are used as landmarks to search for proto-clusters because they are thought to be progenitors of massive elliptical galaxies located in the centers of local galaxy clusters (e.g., McLure et al. 1999). Indeed, some overdensity regions around HzRGs of various galaxy populations such as Lyman  $\alpha$  emitters (LAEs), Lyman break galaxies (LBGs), and distant red galaxies (DRGs), are identified as proto-clusters (e.g., Pentericci et al. 1997; Miley et al. 2004; Kurk et al. 2004a, 2004b; Kajisawa et al. 2006a; Kodama et al. 2007; Kuiper et al. 2010). Therefore, a narrow-band imaging survey targeting  $H\alpha$

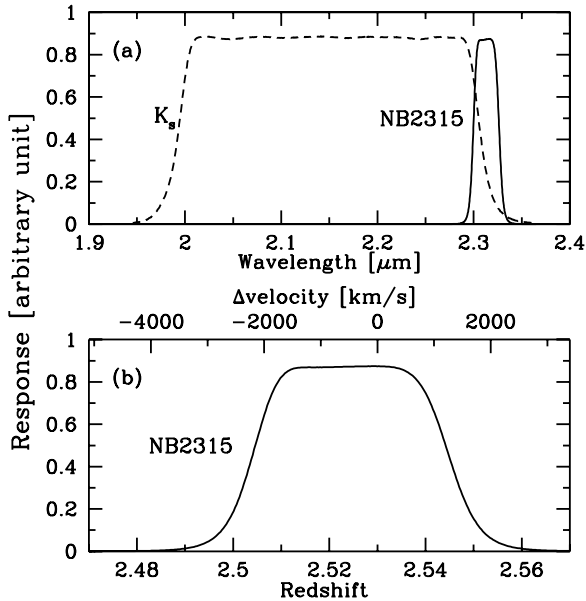


**Figure 1.** (a) The broken line shows a response curve of MOIRCS  $K_s$  broadband filter, and the solid line shows that of MOIRCS NB2315 narrow-band filter ( $\lambda_c = 2.313 \mu\text{m}$ ,  $\Delta\lambda = 0.027 \mu\text{m}$ ). (b) The response curve of NB2315 is shown as a function of redshift. The relative line-of-sight velocity with respect to the radio galaxy redshift ( $z = 2.53$ ) is also shown for the case of the  $H\alpha$  emission line.

emitters (HAEs) around the HzRG is also an effective method for investigating star formation activity in a high- $z$  proto-cluster.

There are already several surveys of  $H\alpha$  emission lines in proto-clusters at  $z \gtrsim 2$ : the PKS 1338-262 proto-cluster at  $z = 2.16$  (Kurk et al. 2004b; Hatch et al. 2011), the 4C+10.48 proto-cluster at  $z = 2.35$  (Hatch et al. 2011), and the 4C23.56 proto-cluster at  $z = 2.48$  (Tanaka et al. 2011). Hatch et al. (2011) found statistical excesses in the number density of  $H\alpha$  emitting galaxies in the vicinity of the radio galaxies of PKS 1338-262 and 4C+10.48 by a factor of  $> 10$  compared with that of general fields. The  $H\alpha$  luminosity functions in the proto-clusters have similar shapes to those in the general fields, but the normalization of the luminosity function in the proto-clusters is a factor of 13 higher than that in the fields. Tanaka et al. (2011) found a statistical excess in the number density of HAEs in the 4C23.56 proto-cluster by a factor of five compared to a general field. Combining with mid-infrared photometric data which traces reradiation by dust, they revealed that active star formation must be occurring in the proto-clusters, which is as active as that in the general fields at similar redshifts. They also suggested that it is probable that star formation activity in proto-clusters gets stronger toward higher redshifts. Therefore, it is interesting to probe star formation activity in higher redshift proto-clusters to confirm this trend.

In this paper, we present results of our  $H\alpha$  emission line survey in the  $4' \times 7'$  region around a radio galaxy USS 1558-003 at  $z = 2.53$  with the NB2315 narrow-band filter ( $\lambda_c = 2.313 \mu\text{m}$ ,  $\Delta\lambda = 0.027 \mu\text{m}$ ). This filter is designed to perfectly match to this particular proto-cluster (Figure 1). The redshift of 2.53 is the highest in which  $H\alpha$  emission lines can be traced by near-infrared imaging on a ground-based telescope. Kajisawa et al. (2006a) and Kodama et al. (2007) reported a statistical excess of bright DRGs around this radio galaxy as evidence for the existence of a proto-cluster associated with the radio galaxy at  $z = 2.53$ . In the current paper, our studies have been conducted under the MAHALO-Subaru project (Mapping

$H\alpha$  and Lines of Oxygen with Subaru; T. Kodama et al., in preparation). This project aims to reveal the environmental dependence of star-forming activities by wide-field narrow-band imaging of  $H\alpha$  or  $[\text{O II}]$  emission lines in (proto-)clusters and general fields at  $1.5 \lesssim z \lesssim 2.5$ . See also to T. Kodama et al. (in preparation) for details, such as the method of selection of emission line galaxies and the estimation of galaxy properties (star formation rates [SFRs] and stellar masses). Our previous studies have demonstrated that narrow-band imaging is very powerful and useful in completely sampling star-forming galaxies with emission lines down to a certain limiting flux (Kodama et al. 2004; Koyama et al. 2010, 2011; Hayashi et al. 2010, 2011; Tadaki et al. 2011; Tanaka et al. 2011).

The structure of this paper is as follows: Observations and available data are described in Section 2. Our sample of HAEs at  $z = 2.53$  around the proto-cluster is selected from the photometric catalog in Section 3. We investigate the spatial distribution and colors of the  $H\alpha$  emitters in Section 4. Discussions on star-forming activity, properties of HAEs on the red sequence, and the  $H\alpha$  emission of the radio galaxy are in Section 5. Finally, we summarize our results in Section 6. Throughout this paper, magnitudes are presented in the AB system, and we adopt the cosmological parameters of  $h = 0.7$ ,  $\Omega_m = 0.3$ , and  $\Omega_\Lambda = 0.7$ . Vega magnitudes in  $J$ ,  $H$ , and  $K_s$ , if preferred, can be obtained from our AB magnitudes using the following calibrations:  $J(\text{Vega}) = J(\text{AB}) - 0.94$ ,  $H(\text{Vega}) = H(\text{AB}) - 1.38$ , and  $K(\text{Vega}) = K(\text{AB}) - 1.86$ , respectively. At  $z = 2.53$ , 1 arcmin corresponds to 0.483 Mpc (physical) and 1.705 Mpc (comoving), respectively.

## 2. OBSERVATION AND DATA

Observations of the USS 1558-003 proto-cluster were conducted on 2011 March 11, April 17 and 29 as a Subaru open-use intensive program (S10B-028, PI: T. Kodama). The optical and near-infrared (NIR) images were taken with the Subaru Prime Focus Camera (Suprime-Cam; Miyazaki et al. 2002) and the Multi-Object Infra-Red Camera and Spectrograph (MOIRCS; Ichikawa et al. 2006; Suzuki et al. 2008) on the Subaru telescope, respectively. The Suprime-Cam has a field of view (FoV) of  $27 \times 34 \text{ arcmin}^2$ , while MOIRCS has an FoV of  $4 \times 7 \text{ arcmin}^2$ . The  $K_s$  and NB2315 data were obtained with two pointings with an offset of  $1'$  in right ascension and  $1'$  in declination, to neatly cover the dense clumps of HAEs (see Section 3.2) that were recognized during the course of observing runs. We refer to these two pointings as F1 and F2. Although the panoramic Suprime-Cam image covers the entire region of both F1 and F2, the MOIRCS  $J$  and  $H$  data are available only in the F2 pointing. Therefore, it should be noted that the area used in this study is limited to the F2 region of about  $4 \times 7 \text{ arcmin}^2$ , where both optical and NIR data are available. The weather was fine during the observations, and the sky condition was photometric. The seeing was less than  $0''.66$  in all the images, except it was  $0''.70$  in the  $B$  band. The total integration times in the optical and NIR broadbands ranged from 45 to 90 minutes. We took significantly longer integration (203 minutes) at the narrow-band NB2315. Consequently, the available data set consists of six items of broadband data,  $B$ ,  $r'$ ,  $z'$  in optical and  $J$ ,  $H$ ,  $K_s$  in NIR, and the narrow-band data with the NB2315 filter.

All of the optical and NIR data are reduced in a standard manner using a data reduction package for Suprime-Cam (SD-FRED ver.2.0; Ouchi et al. 2004) and MOIRCS (MCSRED<sup>5</sup>

<sup>5</sup> <http://www.naoj.org/staff/ichi/MCSRED/mcsred.html>

**Table 1**  
Summary of the Optical and Near-Infrared Images

Filter	FoV <sup>a</sup>	Integration Time (minutes)	Limiting Mag <sup>b</sup> (5 $\sigma$ )	Seeing (arcsec)	Instrument	Observation Date
<i>B</i>	F1+F2	80	27.16	0.70	Suprime-Cam	2011 Apr 29
<i>r'</i>	F1+F2	90	26.87	0.63	Suprime-Cam	2011 Apr 29
<i>z'</i>	F1+F2	55	25.75	0.66	Suprime-Cam	2011 Apr 29
<i>J</i>	F2	75	24.18	0.42	MOIRCS	2011 Mar 11
<i>H</i>	F2	45	23.51	0.47	MOIRCS	2011 Mar 11
<i>K<sub>s</sub></i>	F1+F2	57	23.65	0.66	MOIRCS	2011 Mar 11, 2011 Apr 17
NB2315	F1+F2	(F1: 32, F2: 25) 203	(F1: 23.46, F2: 23.17) 23.01	(F1: 0.66, F2: 0.40) 0.53	MOIRCS	2011 Mar 11, 2011 Apr 17
		(F1: 133, F2: 70)	(F1: 22.74, F2: 22.35)	(F1: 0.53, F2: 0.36)		

**Notes.** Finally, the FWHMs of PSF in all the images are matched to 0''.66, except for the *B*-band image which has an FWHM of 0''.70.

<sup>a</sup> The pointings of F1 and F2 for *K<sub>s</sub>* and NB2315 images have an offset of 1' to the west and 1' to the south.

<sup>b</sup> The limiting magnitudes are measured with a 1''.5 diameter aperture.

by I. Tanaka), respectively. See to Hayashi et al. (2010, 2011) for the details of the reduction procedures. Point-spread functions (PSFs) in all the reduced images, except for the *B*-band image, are matched to 0.66 arcsec. The zero points of magnitudes are determined using the standard stars: GD153 and LDS749B for optical data, and FS27, FS137, and G191-B2B for NIR data. The 5 $\sigma$  limiting magnitudes are 27.16, 26.87, 25.75, 24.18, 23.51, 23.65, and 23.01 in *B*, *r'*, *z'*, *J*, *H*, *K<sub>s</sub>*, and NB2315, respectively, which are measured with a 1''.5 diameter aperture. The details of the observation and data are summarized in Table 1.

### 3. H $\alpha$ EMITTERS IN THE USS 1558-003 PROTO-CLUSTER

#### 3.1. Photometric Catalog

Source detection is performed on the original NB2315 image with an FWHM of PSF of 0''.53 rather than the PSF matched image, using SExtractor (ver. 2.5.0; Bertin & Arnouts 1996), and photometry on all the images is conducted by the double-image mode of SExtractor. Color indices are defined with aperture magnitudes MAG\_APER, which are measured with a 1''.5 diameter aperture, while the total magnitudes are defined with MAG\_AUTO magnitudes which are measured with an elliptical aperture (see also Kron 1980). Magnitude errors are estimated from 1 $\sigma$  sky noise at each object position taking into account slightly different exposure times and sensitivities, which are thus corrected for the difference in depth over the entire FoV. The regions near the edges of each image where the exposure time is shorter than 75% of the total in each combined image are masked. If an object is not detected in a broadband filter, a 2 $\sigma$  limiting magnitude is used to estimate the upper/lower limits in color indices or the upper limits in magnitudes. We make sure that the stellar colors are consistent with those of stellar templates given in Gunn & Stryker (1983) in order to check the zero points of magnitudes. From such comparison, the zero-point magnitudes in *B*, *r'*, *z'*, and *J* are corrected by  $\sim 0.15$  mag at most so that the stellar colors are in good agreement with those of the stellar atlas. Moreover, magnitudes are corrected for the Galactic absorption by the following magnitudes:  $A(B) = 0.62$ ,  $A(r') = 0.41$ ,  $A(z') = 0.23$ ,  $A(J) = 0.14$ ,  $A(H) = 0.09$ ,  $A(K_s) = 0.06$ , and  $A(\text{NB912}) = 0.05$ , which are derived from the extinction law of Cardelli et al. (1989) on an assumption of  $R_V = 3.1$  and  $E(B - V) = 0.155$  based on Schlegel et al. (1998).

As a result, 1035 objects are detected in the NB2315 image at more than the 5 $\sigma$  level (i.e., 23.01 mag in the F1+F2 region). Among them, 754 galaxies are distinguished from 281 stars

based on their *B* - *z'* and *z'* - *K<sub>s</sub>* colors. This method of separating galaxies from stars is devised by Daddi et al. (2004) (see also Kong et al. 2006).

The detection completeness is investigated as follows:<sup>6</sup> First, artificial objects with given magnitudes and Gaussian profiles with FWHM of 0''.53 are distributed on the NB2315 image. Source detection is conducted in the same manner as described above, and then the fraction of detected artificial objects is calculated. The detection completeness is found to be more than 74 (83)% down to 23.0 (22.0) mag in NB2315.

#### 3.2. Selection of H $\alpha$ Emitters

Galaxies with a nebular emission line that happens to enter the NB2315 narrow-band filter should be observed to be much brighter in NB2315 magnitude compared with the *K<sub>s</sub>* broadband magnitude, which samples primarily the underlying continuum flux density. We thus apply the following criteria to select such galaxies with an emission line at  $\sim 2.313 \mu\text{m}$ :

$$K_s - \text{NB} > -2.5 \log \left( 1 - \sqrt{f_{3\sigma, K_s}^2 + f_{3\sigma, \text{NB}}^2 / f_{\text{NB}}} \right) + 0.1, \quad (1)$$

$$K_s - \text{NB} > 0.35, \quad (2)$$

where  $f_{3\sigma}$  is the 3 $\sigma$  sky noise flux in each band and  $f_{\text{NB}}$  is the NB2315-band flux density (Figure 2). The continuum flux density is corrected for a color term by 0.1 mag as given in the rightmost side of Equation (1), because the effective wavelength of the *K<sub>s</sub>* filter is different by 0.163  $\mu\text{m}$  from that of the NB2315 filter (Figure 1). We note that the *K<sub>s</sub>*-NB2315 colors of Coleman et al. (1980) templates redshifted to  $z = 2.53$  are actually distributed around 0.1 mag. The second criterion of  $K_s - \text{NB} > 0.35$  corresponds to the observed equivalent width larger than 79  $\text{\AA}$  (22  $\text{\AA}$  in the rest frame if a galaxy is located at  $z = 2.53$ ) after being corrected for the color term of 0.1 mag. We select galaxies with color excesses in *K<sub>s</sub>*-NB2315 greater than 3 $\sigma$  photometric errors. This means that an emission line with a flux larger than  $2.6 \times 10^{-17} \text{ erg s}^{-1} \text{ cm}^{-2}$  can be firmly detected. If the color excess is due to an H $\alpha$ +[N II] emission line pair at  $z = 2.53$ , the limiting line flux corresponds to  $L(\text{H}\alpha) = 1.1 \times 10^{42} \text{ erg s}^{-1}$  and a dust-free SFR of 8.6  $M_\odot \text{ yr}^{-1}$  (Kennicutt

<sup>6</sup> This completeness refers to point sources, and the one for extended objects can be relatively shallower than that. However, the sizes of galaxies at  $z \sim 2.5$  are not generally large enough to be resolved in the current data, and the assumption of point sources may not be so impractical.

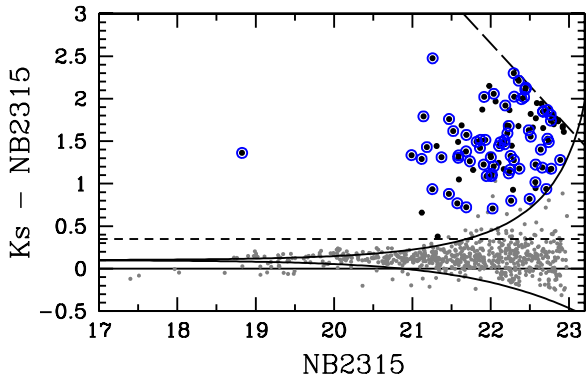


**Figure 2.** Color–magnitude diagram of  $K_s$ –NB2315 vs. NB2315. The solid curves show the boundary of  $3\sigma$  excess given by Equation (1). The broken line shows the  $2\sigma$  limit in  $K_s$ –NB2315 color. The black dots located above the solid curve indicate the NB2315 emitters. Some objects with large enough color excesses are not classified as emitters due to the shallow data at the individual object positions. Blue open circles with black dots represent the  $H\alpha$  emitters associated with the radio galaxy at  $z = 2.53$ , which are identified by the color selection criteria in  $r' - J$  and  $J - K_s$  (Equation [3] and Figure 3).

(A color version of this figure is available in the online journal.)

1998), where the ratio of  $[N II]$  to  $H\alpha$  ( $[N II]/H\alpha$ ) is assumed to be 0.22 (Sobral et al. 2012). We also find 12 galaxies whose line fluxes are larger than this limit, but color excesses are smaller than the  $3\sigma$  level due to their location near the edge of the images where the depth is shallower. These galaxies are not included in our emitter sample. As a result, we select 102 NB2315 emitters out of 754 galaxies over the  $\sim 4 \times 7$  arcmin<sup>2</sup> area (Figure 2).

Although we aim to select HAEs at  $z = 2.53$ , it is possible that some of the emission lines detected with the NB2315 filter are some other lines at different redshifts such as  $H\beta$  or  $[O III]$  at  $z \sim 3.6$ ,  $[O II]$  at  $z = 5.2$ , or Paschen series lines at  $z < 1.0$ . However, it is unlikely that the bulk of the NB2315 emitters originate from  $H\beta$ ,  $[O III]$ , or  $[O II]$  lines at  $z > 3.5$ , because the color excesses of the emitters are quite large as shown in Figure 2. Note that the large color excesses we see in  $K_s$ –NB2315 may correspond to unrealistically large emission line fluxes if they are all located at such high redshifts. Indeed, all but seven NB2315 emitters are detected in the  $B$  band, and 64 out of 68 HAEs classified below also have the detection. If a nebular line detected by the NB2315 filter would be either an  $[O III]$  or an  $[O II]$  line, the line luminosity of  $[O III]$  (or  $[O II]$ ) is larger than  $2.0(4.7) \times 10^{42}$  erg s<sup>−1</sup>, respectively. The luminosity functions of  $[O III]$  at  $z = 0.84$  (Ly et al. 2007) and  $[O II]$  at  $z = 1.47$  (Sobral et al. 2012) imply that no more than one  $[O III]$  or  $[O II]$  emitter with such a high luminosity can be included in our NB2315 emitter sample with limited field coverage, if any. Therefore, we believe that there is little contamination from the lines at  $z > 3.5$  in our NB2315 emitter sample. Moreover, it should be noted that our NB2315 survey targets the plausible proto-cluster at  $z = 2.53$  associated with the radio galaxy, and we must be preferentially detecting HAEs at  $z = 2.53$  rather than other high- $z$  emitters in the general field. However, as reported by Geach et al. (2008), who conducted  $H_2S1$  narrow-band ( $\lambda_c = 2.121 \mu\text{m}$ ) imaging with WFCAM on UKIRT to search for HAEs at  $z = 2.23$  in the COSMOS field, other lower- $z$  emission lines such as  $Pa\alpha$  and  $Pa\beta$  at  $z < 1$  can be significant contaminations. In order to discriminate  $H\alpha$  from other lower- $z$  contaminant lines, we set the following color selection criteria on the color–color diagram,  $r' - J$  versus  $J - K_s$ :

$$\begin{aligned} J - K_s > 0.7(r' - J) + 0.05 & \quad \text{for } r' - J < 1.9 \\ J - K_s > 1.38 & \quad \text{for } r' - J > 1.9. \end{aligned} \quad (3)$$

This classification with  $r'JK_s$  colors is an analog of the  $BzK$  color selection of galaxies at  $1.4 \lesssim z \lesssim 2.5$  devised by Daddi et al. (2004), but it is optimized to identify galaxies at  $z \gtrsim 2.5$ . Figure 3 shows the color tracks of model spectra with various star formation histories and fixed formation redshift of  $z_f = 5$  based on Bruzual & Charlot (2003), and four spectral energy distribution (SED) templates in Coleman et al. (1980), which are redshifted from  $z = 0.0$  to  $z = 4.0$ . This figure suggests that the criteria enable us not only to select DRGs as galaxies with red colors ( $J - K_s(\text{vega}) > 2.3$ ), but also to isolate star-forming galaxies at  $z \gtrsim 2.5$  from those at lower redshifts. Although no dust extinction is taken into account for the color tracks, the arrow in the figure shows the reddening vector of  $E(B - V) = 0.2$  based on the Calzetti et al. (2000) extinction curve. This indicates that our selection criteria are relatively free from the dust reddening effect, as the vector is almost parallel to the slanted boundary line. Indeed, a group of emission line galaxies that are likely to be  $H\alpha$  emitters at  $z = 2.53$  seems to be located separately from the bulk of galaxies at lower redshifts as shown in the right panel of Figure 3. Thus, our selection criteria work well to select  $H\alpha$  emitters at  $z = 2.53$ .

We attempt to apply other color selection methods such as the original  $Bz'K_s$  selection (Daddi et al. 2004) and  $JHK_s$  selection (Kajisawa et al. 2006a; Kodama et al. 2007). However, the  $Bz'K_s$  selection is effective for selecting galaxies at  $1.4 \lesssim z \lesssim 2.5$ , while we aim to pick out HAEs at  $z \sim 2.5$  among the NB2315 emitters. Since they are located just at the upper edge of the redshift range of the  $Bz'K$  selection, the selection of HAEs may well be quite incomplete. On the other hand, it is found that the  $JHK_s$  selection does not work well due to the shallowness of  $H$ -band data and the incompleteness in the selection of blue star-forming galaxies. Therefore, we judge that the classification with  $r'JK_s$  colors works best among them to identify HAEs at  $z = 2.53$ . Instead of the color selection, one may consider the use of photometric redshifts to discriminate among different emission lines at different redshifts. We also derive photometric redshifts of our NB2315-detected galaxies using six-band photometry of  $B, r', z', J, H, K_s$  and the EAZY code (Brammer et al. 2008). However, we find that it is difficult to clearly discriminate HAEs from other possible lines, especially those at  $z > 1.0$ , based on the photometric redshifts. In the end, we decide to use the  $r'JK_s$  diagram to identify HAEs. Consequently, we select 68 HAEs in total (Figure 3).

### 3.3. Selection of Distant Red Galaxies

DRG is a class of galaxy populations at  $2 \lesssim z \lesssim 4$  with red colors of  $J - K_s > 1.38$  or  $J - K_s(\text{vega}) > 2.3$  (Franx et al. 2003) which consist of dusty starburst galaxies and quiescent galaxies. To select such red galaxies in this region, the DRG color selection is applied to the  $K_s$ -selected catalog, which is made with the same procedures as those described in Section 3.1, except that source detection is performed on the  $K_s$  image. The  $K_s$ -selected catalog is used only for the selection of DRGs, since such a catalog enables us to select DRGs more completely down to fainter magnitudes than the NB2315-limiting magnitude. The catalog includes 1340 objects brighter than  $5\sigma$  limiting magnitude in  $K_s$ . Among them, 1002 objects are classified as galaxies, while the remaining 338 objects are classified as stars. Consequently, 42 DRGs are selected from the  $K_s$ -selected catalog. It is expected that red galaxies associated with the proto-cluster at  $z = 2.53$  tend to be seen as DRGs, although DRGs in general can be located in a much wider redshift range of  $2 \lesssim z \lesssim 4$ .

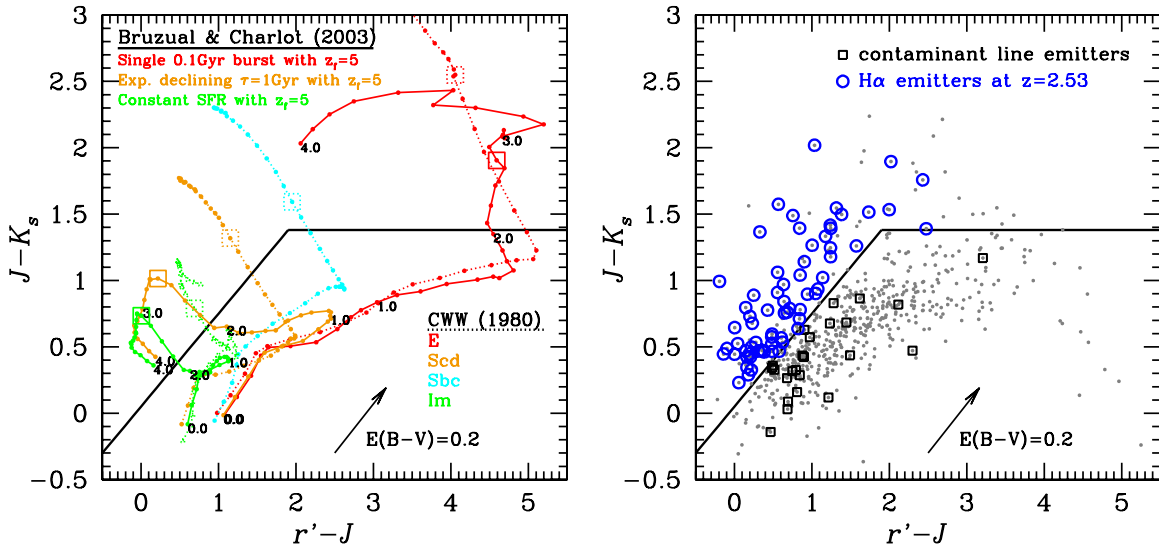


**Figure 3.** Left panel: color-color diagram of  $r' - J$  vs.  $J - K_s$ . The red, orange, and green solid lines show color tracks of model SEDs for three types of star formation histories with a fixed formation redshift of  $z_f = 5$  based on Bruzual & Charlot (2003). The dotted lines show the color tracks created by four empirical spectral templates from elliptical to irregular type galaxies compiled by Coleman et al. (1980). Dust extinction is not corrected, but the absorption by neutral hydrogen given by Madau (1995) is taken into account. The arrow shows a reddening vector of  $E(B - V) = 0.2$ , which is estimated from the dust extinction curve of Calzetti et al. (2000). The numbers shown along the tracks for the Bruzual & Charlot (2003) model indicate redshifts, and the open squares correspond to  $z = 2.5$ . The black folded solid line shows the boundaries of our selection criteria to identify  $H\alpha$  emitters among the NB2315 emitters (Equation [3]). Right panel: same as the left panel, but the observed galaxy colors are plotted. The gray dots show the NB2315-detected galaxies. The blue open circles show our sample of  $H\alpha$  emitters, and black open squares show the other contaminant line emitters probably located at lower- $z$  ( $z < 1$ ).

(A color version of this figure is available in the online journal.)

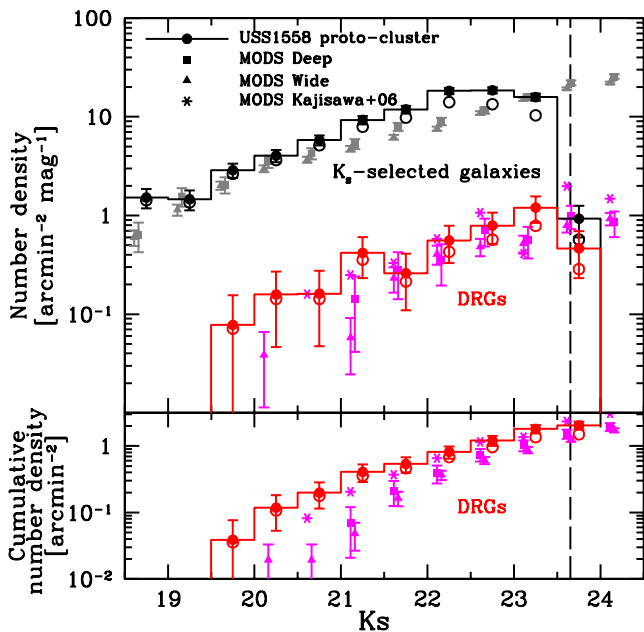


**Figure 4.** Differential number densities of DRGs and  $K_s$ -selected galaxies around the USS 1558-003 proto-cluster are shown in the upper panel, and cumulative number densities of DRGs are shown in the lower panel. Filled circles show the number densities corrected for detection incompleteness, while open circles show those without corrections. The filled squares and triangles show the results obtained by MODS deep and wide surveys (Kajisawa et al. 2011), and asterisks show those of Kajisawa et al. (2006b). The results of MODS deep and wide surveys are not corrected for detection incompleteness. Error bars are estimated based on Poisson statistics. The vertical broken line shows the  $5\sigma$  limiting magnitude in  $K_s$ .

(A color version of this figure is available in the online journal.)

Figure 4 shows the number densities of DRGs and  $K_s$ -selected galaxies which are corrected for detection incompleteness estimated in the same manner as in Section 3.1. For comparison with other studies, we also plot the results of the general blank

field survey, the MOIRCS Deep Survey (MODS; Kajisawa et al. 2006b, 2011) where the deep and wide surveys have FoVs of 28.2 and 103.3 arcmin<sup>2</sup>, respectively. The number densities of DRGs as well as  $K_s$ -selected galaxies in the USS1558 proto-cluster do not show strong overdensities compared to those in the MODS, although some excesses by a factor of a few are seen at several bins. Kodama et al. (2007) found that this region shows an overdensity of bright DRGs compared to the GOODS-S field (Giavalisco et al. 2004). Figure 4 indeed shows that there is an excess of bright DRGs with  $K_s \lesssim 21.5$  in the USS 1558-003 proto-cluster that are almost absent in the general blank field. The difference in number densities of DRGs between the proto-cluster and the general field is clearer in the cumulative densities, showing an excess at  $\sim 2\sigma$  level in the bin with  $K_s < 21.5$ . Moreover, the spatial distribution of DRGs is not homogeneous but is rather clustered around the radio galaxy (see Section 4.1). The fact that there is no significant excess of faint DRGs in the proto-cluster region may suggest that most of the faint member galaxies in this proto-cluster have bluer colors, probably due to ongoing star formation activities, and that passive red galaxies would be gradually emerging later on. Although we do not yet have any spectroscopic confirmation of membership of the DRGs except for the radio galaxy itself, it is likely that the region around the USS 1558-003 radio galaxy is a proto-cluster at  $z = 2.53$ .

## 4. RESULTS

### 4.1. Spatial Distribution of $H\alpha$ Emitters

Figure 5 shows the spatial distribution of our 68 HAE candidates associated with the USS 1558-003 radio galaxy at  $z = 2.53$  located at (0,0) in the figure. The 42 DRGs are also plotted with red filled circles. We find that there are three outstanding regions where HAEs and/or DRGs are strongly clustered, which we hereafter call clump-1, clump-2, and clump-3. In fact, as summarized in Table 2, the number densities

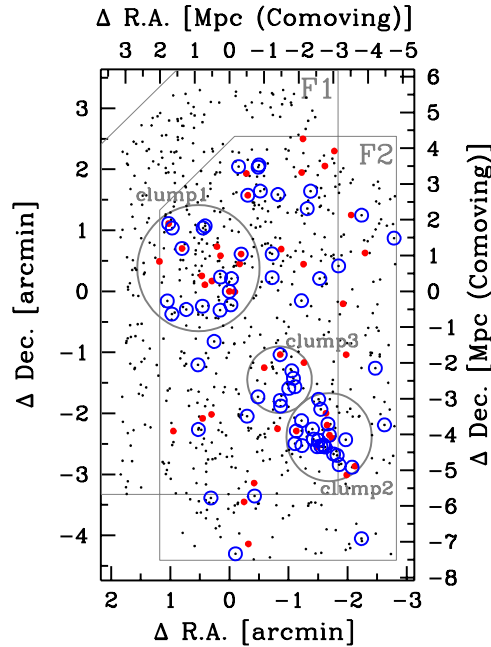


**Figure 5.** Spatial distribution of  $H\alpha$  emitters. The blue open circles show  $H\alpha$  emitters at  $z = 2.53$ . The red filled circles show DRGs, and black dots are NB2315-detected galaxies. North is up, and east is to the left. The origin of the coordinates is the position of the USS 1558-003 radio galaxy. The three gray circles are the regions where  $H\alpha$  emitters and DRGs are strongly clustered, which are defined as clump-1, clump-2, and clump-3, respectively. The two regions enclosed by gray solid lines show our MOIRCS pointings (F1 and F2). (A color version of this figure is available in the online journal.)

of HAEs and DRGs in these three clumps are all higher than those of averaged values across the observed fields by factors of two to five for HAEs and two to three for DRGs. Clump-1 is in the vicinity of the radio galaxy, and it contains both HAEs and DRGs around the radio galaxy. If we assume that the central dominant radio galaxy grows to a cD galaxy in the future, this region may correspond to the central part of the cluster. The fact that DRGs are also clustered in this clump may also suggest that this part of the proto-cluster is the oldest. Clump-2 is the most conspicuous, densest association of the HAEs and DRGs, and it is located at  $\sim 3/2$  (about 1.5 Mpc in physical scale) away from the radio galaxy to the southwest. Clump-3 is a smaller group of HAEs located between clump-1 and clump-2.

It is interesting to note that the HAEs are more strongly clustered toward the southwest clumps (clump-2 and clump-3) rather than in the immediate surrounding region around the radio galaxy (clump-1). They constitute a part of the large-scale structure hosting the radio galaxy and clump-1, and they would all merge together in the near future to form a more massive single cluster around the radio galaxy. It is obvious that this proto-cluster region is not yet relaxed and is just in the process of galaxy assembly from the surrounding regions. We note that such distribution of the  $H\alpha$  emitters is similar to that of DRGs reported by Kodama et al. (2007) based on NTT/SOFI imaging data. In fact, we also confirm that the DRGs tend to be located in and along the structures traced by the  $H\alpha$  emitters, based on our deeper MOIRCS data (Figure 5). Furthermore, we find that these DRGs also meet the  $BzK$  criteria which select galaxies primarily at  $1.4 \lesssim z \lesssim 2.5$ , suggesting that a significant number of these DRGs are likely to be physically associated with the proto-cluster hosting the radio galaxy at  $z = 2.53$ .

The three clumps in the 1558-003 proto-cluster host a large number of HAEs. The surface number density of HAEs in the

**Table 2**  
The Number and Number Density of HAEs and DRGs

Region	Area (arcmin <sup>2</sup> )	Number		Density (arcmin <sup>-2</sup> )	
		HAE	DRG	HAE	DRG
Clump 1	3.36	15	12	$4.46 \pm 1.15$	$3.57 \pm 1.03$
Clump 2	1.64	20	8	$12.2 \pm 2.73$	$4.88 \pm 1.72$
Clump 3	0.94	8	3	$8.51 \pm 3.01$	$3.19 \pm 1.84$
All clumps	5.94	43	23	$7.24 \pm 1.10$	$3.87 \pm 0.81$
Others	21.16	25	19	$1.18 \pm 0.24$	$0.90 \pm 0.21$
Entire field	27.10	68	42	$2.51 \pm 0.30$	$1.55 \pm 0.24$

**Notes.** Errors in number density are estimated based on Poisson statistics.

three clumps is  $\sim 37 \pm 13$  times larger than those in the redshift slice at  $z = 2.2$  in the GOODS-North field ( $H\alpha$  emission survey with NB209 narrow-band filter; Tadaki et al. 2011). Similarly, we also find that it seems that the surface number density is  $\sim 14 \pm 3$  and  $17 \pm 4$  times larger than those in the redshift slices of  $z = 2.2$  and  $2.53$  in the SXDS field ( $H\alpha$  emission survey with NB209 and NB2315; K.-I. Tadaki et al., in preparation).

Tanaka et al. (2011) conducted an HAE survey in the field around the 4C 23.56 radio galaxy at  $z = 2.48$  with a CO narrow-band filter on MOIRCS; they found 11 HAE candidates to flux down to  $\sim 7.5 \times 10^{-17}$  erg s<sup>-1</sup> cm<sup>-1</sup> and rest-frame EW > 50 Å over a 23.6 arcmin<sup>2</sup> area, which is similar to our survey area. It is found that HAEs are distributed on the east side of the radio galaxy 4C 23.56, and there is a clump of HAEs  $\sim 2$  Mpc (in comoving scale) away from the radio galaxy. Such an offset distribution of HAEs from the radio galaxy is similar to that in our USS 1558-003 field, although our  $H\alpha$  emitters are more strongly clustered than the 4C 23.56 field. However, note that the EW cut and the limiting flux used for HAE selection are slightly different in our survey than in Tanaka et al. (2011). Our survey enables us to sample HAEs with fainter line fluxes and smaller EWs. If we apply the same EW cut and the limiting flux as in Tanaka et al. (2011) to our sample in the USS 1558-003 field, the number of HAEs reduces to 27, but it is still considerably larger than that in the 4C 23.56 field. The discovery of clumps of HAEs in these proto-clusters around the radio galaxy at  $z \sim 2.5$  clearly indicates that we are witnessing the process of mass assembly of clusters at their early stage when galaxies are vigorously assembling to form dense cluster cores while they are actively forming stars.

Moreover, Hatch et al. (2011) reported the studies for two proto-clusters around the radio galaxies MRC 1138-262 at  $z = 2.16$  and 4C+10.48 at  $z = 2.35$ . These studies suggested that proto-clusters at  $z \gtrsim 2$  tend to show a statistical excess of HAEs compared to the general fields at similar redshifts. However, they found that  $H\alpha$  emitters in the 4C+10.48 region are not strongly clustered, while those in the MRC 1138-262 region are clustered (see Kurk et al. 2004b). Moreover, both proto-clusters show inhomogeneous spatial distribution of HAEs around each radio galaxy, and most of the  $H\alpha$  emitters are distributed only on one side of the radio galaxies, similar to 4C 23.56 (Tanaka et al. 2011) and USS 1558-003 (this study).

Another interesting result we find is that the radio galaxy shows an extremely extended  $H\alpha$  emission spatially as shown in Figure 6. In the NB2315 image, we can note that the structure of the  $H\alpha$  emission is stretched in the northeast–southwest direction. The size of the  $H\alpha$  emission is  $\sim 4/5$ , which corresponds to  $\sim 36$  kpc in physical scale. We discuss the extended  $H\alpha$  emission of radio galaxy itself in Section 5.2.

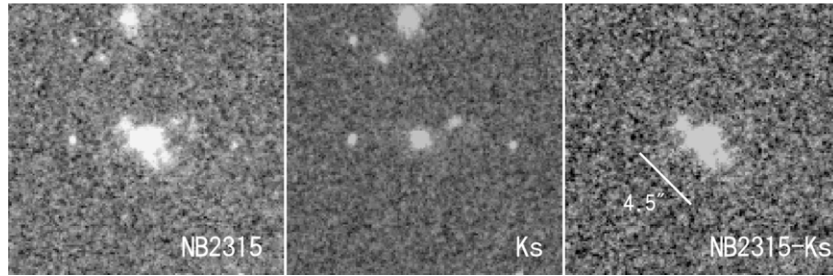


**Figure 6.** Close-up views of the USS 1558-003 radio galaxy at  $z = 2.53$  in the NB2315,  $K_s$ , and NB2315- $K_s$  images. Note that the FWHM values of PSF in these  $K_s$  and NB2315 images are  $0''.40$  and  $0''.36$ , respectively, since these images are created by combining only the frames taken under excellent seeing conditions  $\sim 0''.4$ . The length of the bar in the NB2315- $K_s$  image indicates the angular size of  $4''.5$ , which corresponds to 36.2 kpc in physical scale. The NB2315- $K_s$  image clearly indicates that the radio galaxy has an extremely extended H $\alpha$  emission.

#### 4.2. Color–Magnitude Diagram

The color–magnitude diagram is a powerful tool for investigating the properties of galaxies in clusters or proto-clusters. It is well known that galaxy clusters at low redshifts are dominated by quiescent galaxies which make up the red sequence on the color–magnitude diagram. The tight sequence of red galaxies is one of the prominent features seen in galaxy clusters. However, when and how do such red quiescent galaxies form and evolve? The answer to this question still remains unclear, although there is some evidence suggesting that the blue star-forming galaxies in the early universe evolve and become red quiescent galaxies in high density regions during the redshift interval of 2–3 (e.g., Kajisawa et al. 2006a; Kodama et al. 2007; Kriek et al. 2008; Doherty et al. 2010; Gobat et al. 2011). To address this, it is essential to investigate further the color–magnitude diagram for galaxy cluster and proto-cluster at high redshifts when the clusters are vigorously evolving.

Figure 7 shows a color–magnitude diagram of  $J - K_s$  versus  $K_s$  for the galaxies in the observed field toward the proto-cluster USS 1558-003. The HAEs associated with the proto-cluster are plotted by open circles. As presented by Kodama et al. (2007), we may be able to recognize a sequence of DRGs at  $J - K_s \sim 1.5$ , which corresponds to the color of quiescent galaxies with formation redshift of  $3 \gtrsim z_f < 4$  (Kodama et al. 1998), as indicated by the tickmarks in the figure. It is not surprising that the majority of the HAEs are located on the bluer side of the diagram. However, it is intriguing that some HAEs have very red colors satisfying the DRG criterion and constitute mainly the faint end of the red sequence. We also note that there is a significant color scatter among the red HAEs. Similarly, red HAEs and dusty star-forming galaxies have also been recognized by recent observations of clusters at lower redshifts (Geach et al. 2006; Koyama et al. 2010, 2011). They tend to be dusty star-forming galaxies and are considered to be in the transition phase from active star-forming galaxies to passive quiescent galaxies, probably under the influence of some environmental effects, because these are preferentially found in the medium density regions of galaxy clusters at intermediate redshifts ( $z \lesssim 0.8$ ) when and where we see a sharp transition in the distribution of galaxy colors from blue to red (Tanaka et al. 2005; Koyama et al. 2008). Therefore, it is suggested that the faint end of the red sequence is just being built by those transitional galaxies recognized as the red HAEs.

For a galaxy at  $z = 2.53$ , its  $K_s$ -band luminosity is still a good proxy for the stellar mass. However, the mass-to-luminosity ratio ( $M_*/L_{K_s}$ ) is dependent on SED, and it should be corrected to get a more precise stellar mass from the  $K_s$ -band luminosity. We use a simple method to estimate stellar masses

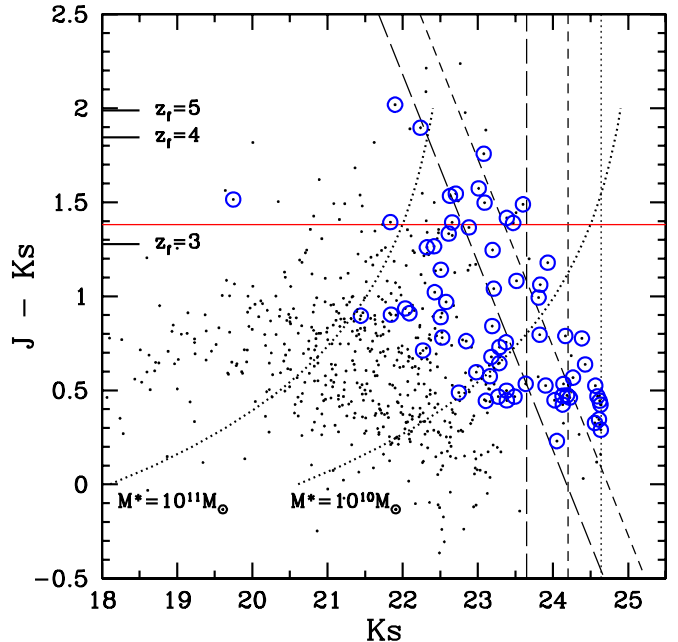


**Figure 7.** Color–magnitude diagram of  $J - K_s$  vs.  $K_s$ . The blue open circles show H $\alpha$  emitters at  $z = 2.53$ , and the black dots show all the galaxies in the observed field. The long-dashed, short-dashed, and dotted lines show  $5\sigma$ ,  $3\sigma$ , and  $2\sigma$  limits in color and magnitude. The red solid horizontal line shows the color corresponding to  $J - K_s = 1.38$ , which is a criterion for selecting DRGs. The  $J - K_s$  colors of the red quiescent galaxies with formation redshifts of  $z_f = 3, 4, \text{ and } 5$  are shown by the tickmarks at the left edge, which are estimated by the Kodama et al. (1998) model. The dotted curves show the isostellar mass curves for  $1 \times 10^{11} M_\odot$  and  $1 \times 10^{10} M_\odot$ , respectively.

(A color version of this figure is available in the online journal.)

of the HAEs based on their  $K_s$ -band magnitudes and  $J - K_s$  colors. The relationship between  $J - K_s$  colors and  $M_*/L_{K_s}$  is approximately estimated using the stellar population synthesis model of Kodama et al. (1998, 1999), where we constructed a sequence of models with varying bulge-to-disk ratios. We note here that because of the SED degeneracy among age, metallicity, and dust extinction, the relationship between  $J - K_s$  and  $M_*/L_{K_s}$  is relatively insensitive to the detailed modeling of stellar populations except for the effect of initial mass function (IMF) variation. We here assume the Salpeter (1955) IMF, and the stellar masses in the models are scaled accordingly. From this experiment, we establish the following relationship between stellar mass ( $M_*$ ),  $K_s$  magnitude, and  $J - K_s$  color:

$$\log_{10}(M_*/10^{11} M_\odot) = -0.4(K_s - K_{11}) + \Delta \log_{10} M, \quad (4)$$

where  $K_{11}$  is the  $K_s$ -band total magnitude corresponding to the stellar mass of  $10^{11} M_{\odot}$  for a passively evolving galaxy formed at  $z = 5$  and observed at  $z = 2.53$ , which is estimated to 22.41. The mass-to-luminosity ratio is corrected for depending on the  $J - K_s$  color by

$$\Delta \log_{10} M = 0.12 - 1.84 \cdot \exp(-1.35 \cdot (J - K_s)). \quad (5)$$

The isostellar mass curves of  $1 \times 10^{11} M_{\odot}$  and  $1 \times 10^{10} M_{\odot}$  are shown in Figure 7. All the HAEs but the radio galaxy have stellar masses of  $\lesssim 10^{11} M_{\odot}$ . Among them, the bluest HAEs with  $J - K_s < 0.7$  are less massive galaxies with stellar masses of  $\lesssim 10^{10} M_{\odot}$ . This gives a dichotomy in the distribution of star-forming galaxies on the stellar mass–color plane, separated at  $\sim 10^{10} M_{\odot}$ , below which the emitters are the bluest and hence the youngest or the most actively star forming.

It should also be noted that the brightest HAE is the radio galaxy, and it is located at the brightest end of the red sequence. Note that similar results are also found in other proto-clusters at  $z = 2-2.5$  (Tanaka et al. 2011; Hatch et al. 2011). Its stellar mass is estimated to be  $\sim 10^{12} M_{\odot}$ , which is typical for HzRGs (e.g., Rocca-Volmerange et al. 2004; Seymour et al. 2007; Hatch et al. 2009). Since the radio galaxy hosts an AGN, it is not straightforward to quantify its SFR from the emission line strength, as it is affected by photoionization by AGNs (Section 5.2).

### 4.3. Star Formation Activity

$H\alpha$  luminosity is a good indicator of SFR in the individual galaxy because the  $H\alpha$  emission line is originated from the photoionization by young O and B stars; thus, it probes the instantaneous star formation activity on a timescale of  $< 20$  Myr. The advantage of using the  $H\alpha$  line to estimate SFR is that it is well calibrated and widely used in studies of galaxies in both the local and high- $z$  universe. Moreover, it is relatively insensitive to dust extinction compared to [O II] and UV luminosities.

$H\alpha$  luminosity is estimated from the emission line flux entering into the narrow-band NB2315, which in most cases is the combination of  $H\alpha$  and [N II] lines. Since the emission lines do not enter the broadband filter for the HAEs at  $z = 2.53$ , as shown in Figure 1, the flux densities in the narrow-band and the broadband filters are expressed as  $f_{\text{NB}} = f_{\text{continuum}} + F(H\alpha + [\text{N II}])/\Delta_{\text{NB}}$  and  $f_{\text{BB}} = f_{\text{continuum}}$ ; thus, the emission line flux is

$$F(H\alpha + [\text{N II}]) = (f_{\text{NB}} - f_{\text{BB}}) \cdot \Delta_{\text{NB}}, \quad (6)$$

where  $\Delta_{\text{NB}} = 271 \text{ \AA}$  is FWHMs of the filters and  $f_{\text{continuum}}$  is the flux density of the continuum level of a spectrum. It should be noted that the fluxes are derived under the assumption that the emission lines are shifted into the center of the narrow-band filter. Since the response curve of the filter is not perfectly top hat (Figure 1), the fluxes can be underestimated if the emission lines are not located in the center of the filter. In that case, the SFR derived from the flux can be a lower limit. The contribution of [N II] is removed from the line flux,  $F(H\alpha + [\text{N II}])$  by assuming the relation between the ratio of [N II]/ $H\alpha$  and the rest-frame equivalent width of  $\text{EW}_0(H\alpha + [\text{N II}])$  given by Sobral et al. (2012).

We derive SFR from  $H\alpha$  flux using the Kennicutt (1998) relation, where  $H\alpha$  flux is corrected for dust extinction using the SFR-dependent calibration given by Garn et al. (2010). The dust extinction correction is important even for the  $H\alpha$  line, which is located in the rest-frame optical wavelength ( $\lambda 6563$ ).

It is often assumed that the amount of dust extinction,  $A(H\alpha)$ , is unity in many papers. However, we adopt the Garn et al. (2010) relation to more realistically estimate the intrinsic  $H\alpha$  luminosity. The specific SFR is also calculated by dividing the SFR by the stellar mass estimated in Section 4.2.

Figure 8 shows SFRs of the HAEs as a function of stellar mass, where dust-uncorrected and dust-corrected SFRs ( $\text{SFR}_{\text{corr}}$ ) are shown in separate panels. There is a correlation that more massive galaxies tend to have higher SFRs, but the dependence is weak because there is significant scatter in SFR for a given stellar mass. A large fraction of the HAEs have high  $\text{SFR}_{\text{corr}}$  larger than  $100 M_{\odot} \text{ yr}^{-1}$ , meaning that many star-forming galaxies in this proto-cluster are in the starburst phase. The object with the stellar mass of  $\sim 10^{12} M_{\odot}$  is the radio galaxy USS 1558-003, and it apparently shows a considerably high SFR. However, this value must be wrong because its  $H\alpha$  line intensity is severely contaminated by the AGN component. In the right panel of Figure 8, we plot the main sequence of star-forming galaxies at  $z \sim 2$  (Daddi et al. 2007). In Rodighiero et al. (2011), the galaxies whose SFRs are more than four times larger than those on the main sequence for a given stellar mass were defined as starburst galaxies. Following this definition, a large fraction of galaxies with  $< 10^{10} M_{\odot}$  are starburst galaxies, while the massive galaxies are more or less located around the main sequence. This is somewhat expected considering the fact that less massive galaxies show the bluest colors on the color–magnitude diagram (Figure 7). In contrast, none of the massive galaxies show such blue colors. It should be noted, however, that the red HAEs with stellar masses larger than  $10^{10} M_{\odot}$  are subject to a large amount of dust attenuation; thus, they are actually in the dusty starburst phase, as we will discuss later in Section 5.1. Figure 9 shows specific SFRs of the HAEs plotted as a function of stellar mass. This indicates that specific SFR and stellar mass are anti-correlated, as seen in many other studies. Massive galaxies have lower SFRs for a given stellar mass compared to less massive galaxies, indicating that star-forming activities have been somewhat truncated and weakened in massive galaxies.

In Figures 8 and 9, HAEs in the three clumps are marked with open circles, squares, and triangles. It appears that the HAEs in clump-2 (i.e., the southwest clump  $\sim 1.5$  Mpc away from the radio galaxy) tend to have higher SFRs than those in other regions. To investigate more quantitatively any environmental dependence in the properties of HAEs, we show in Figure 10 the differential histograms of SFRs, specific SFRs, and stellar masses of the HAEs divided by the regions in the left panels, and their cumulative and normalized number counts in the right panels.

There is no large difference in the distribution of all these physical quantities among different regions in general, except for the weak tendency that SFRs in clump-2 may be slightly higher. In fact, the median SFR of HAE in clump-2 is  $152 M_{\odot} \text{ yr}^{-1}$  which is compared to  $97 M_{\odot} \text{ yr}^{-1}$  in the clump-1,  $99 M_{\odot} \text{ yr}^{-1}$  in the clump-3, and  $106 M_{\odot} \text{ yr}^{-1}$  in the other regions. However, the Kolmogorov–Smirnov test that is applied on the top right panel suggests that the difference does not show high enough statistical significance. The probability of accepting the hypothesis that the SFRs in these clumps have different distributions is less than  $2\sigma$  at most. Therefore, we may conclude that star formation activity at this high redshift ( $\sim 2.5$ ) is high everywhere regardless of environment, not only in the low density outskirts but also in the dense clumps of the proto-cluster. Because we are targeting a proto-cluster and its surrounding

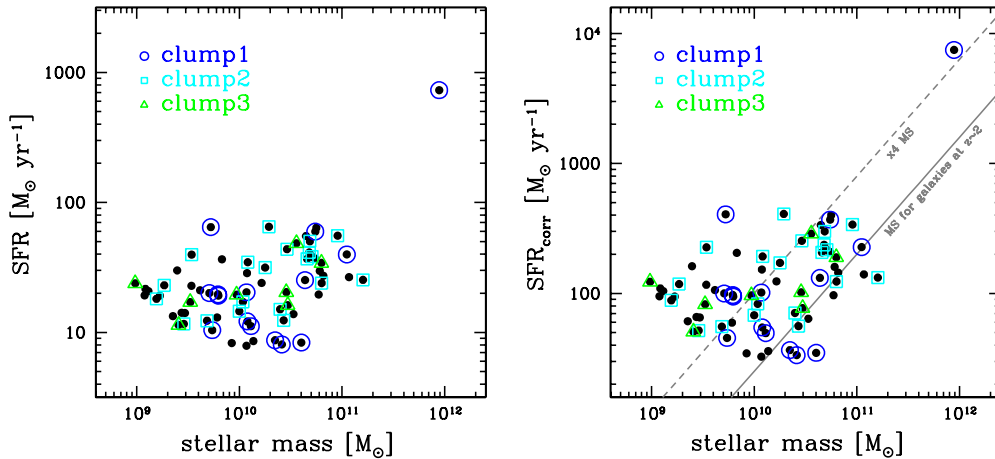


**Figure 8.** Left panel: dust extinction uncorrected SFRs of the 68  $H\alpha$  emitters as a function of stellar mass. Those in clump-1, clump-2, and clump-3 are marked by blue open circles, cyan open squares, and green open triangles, respectively. Right panel: same as the left panel, but the SFRs are corrected for dust extinction (see the text for details). The solid line shows a main sequence (MS) of star-forming galaxies at  $z \sim 2$  (Daddi et al. 2007; Rodighiero et al. 2011), and the broken line corresponds to the SFRs elevated by a factor of four compared to the MS for a given stellar mass.

(A color version of this figure is available in the online journal.)

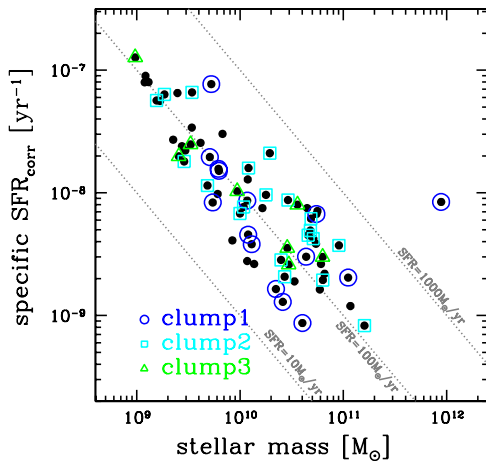


**Figure 9.** Specific SFRs of the  $H\alpha$  emitters as a function of stellar mass. Dust extinction is corrected (see the text for details). The symbols are the same as in Figure 8. The three dotted lines correspond to the constant SFRs of 10, 100, and  $1000 M_{\odot} \text{ yr}^{-1}$ , respectively.

(A color version of this figure is available in the online journal.)

region, it is yet unknown whether such absence of environmental dependence at  $z \sim 2.5$  is universal from one proto-cluster to another, as well as in the general low density fields which are not in the vicinity of proto-clusters.

Furthermore, it is interesting to know how much star formation activity and stellar mass are confined in this proto-cluster region as a whole, as most of the structures and the HAEs are likely to assemble to form a single richer cluster at later times. The integrated stellar mass and SFR of the HAEs in each clump and those in the entire region are shown in Table 3. The uncertainties in the integrated stellar mass and SFR originated from photometric errors are small enough to not greatly influence the discussions below. Also, in this analysis we exclude the most massive radio galaxy in clump-1 ( $\sim 1 \times 10^{12} M_{\odot}$ ), since its  $H\alpha$  line flux is severely contaminated by the AGN component. The integrated stellar mass of DRGs associated with the proto-cluster is derived by subtracting the component of DRGs outside the cluster but projected along the line of sight. Here we use the number count of DRGs in the MODS general field

survey (Kajisawa et al. 2006b, 2011). We note that the total stellar masses estimated here should be taken as the lower limits because we miss less massive galaxies fainter than our observational limits. All clumps but clump-3 have a total stellar mass of  $\sim 10^{12} M_{\odot}$ , while clump-3 has a factor of  $\sim 10$  lower mass of  $\sim 10^{11} M_{\odot}$ . The integrated specific SFR of clump-1 is slightly lower than those of clump-2 and clump-3, by factors of 1.6 and 3.9, respectively, which might suggest that the star formation activity per unit of stellar mass is slightly lower in the closest vicinity of the radio galaxy which may grow to the center of the cluster in the future and that the age of the system is slightly older than the other clumps. However, the statistics are again too poor for us to say anything conclusive yet.

## 5. DISCUSSIONS

### 5.1. Red $H\alpha$ Emitters

As described in Section 4.2, there are some HAEs with colors redder than  $J - K_s = 1.38$ . Figure 11 shows the distribution of the HAEs and DRGs, where the red HAEs with  $J - K_s > 1.38$  are marked by red open circles. It seems that the red HAEs are clustered around the radio galaxy (clump-1) and in the southwest clumps (clump-2 and clump-3). Such concentration of the red emitters in high density regions is qualitatively different from what is seen in the lower redshift cluster at  $z \sim 0.8$  where red HAEs prefer medium density regions, as mentioned in Section 4.2. This may indicate that, in this proto-cluster at  $z \sim 2.5$ , the transition of galaxies is occurring in the densest environment rather than in the outskirts. We note that most of the red HAEs are less massive than  $10^{11} M_{\odot}$  as shown in Figure 7. If the dusty starburst phase does not last so long, these red HAEs would stay on the relatively faint end of the red sequence even after they quench star formation. If the DRGs without  $H\alpha$  emission lines with stellar masses of a few  $\times 10^{11} M_{\odot}$  are really proto-cluster members, the active phase of these massive quiescent galaxies should have been seen at  $z \gtrsim 3$ . Some of their progenitors would be like the populations of LBGs or LAEs, which are in fact often identified in overdense regions (proto-clusters) at  $z \gtrsim 3$  (e.g., Steidel et al. 1998; Miley et al. 2004; Venemans et al. 2005, 2007; Ouchi et al. 2005; Kuiper et al. 2011).

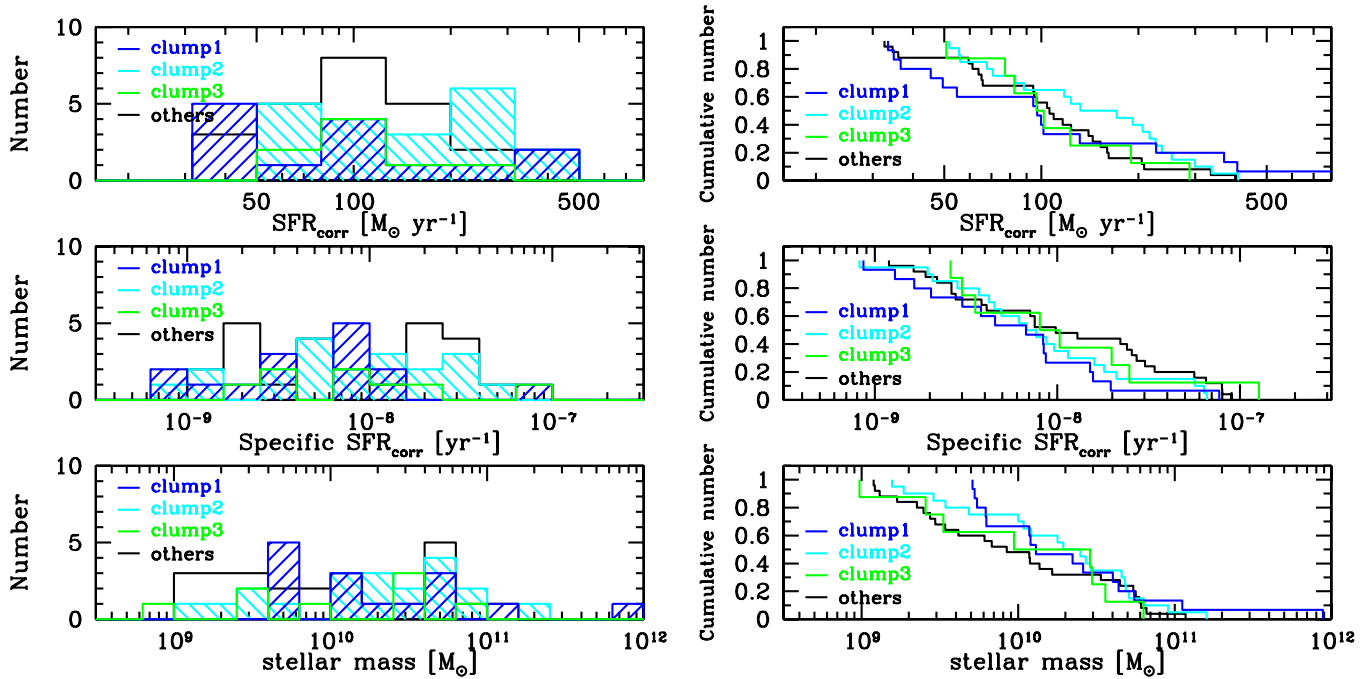


**Figure 10.** Left panels: distribution of SFR (top), specific SFR (middle), and stellar mass (bottom) for the  $H\alpha$  emitters in clump-1 (blue), clump-2 (cyan), clump-3 (green), and the other region (black), respectively. Right panels: normalized cumulative number counts of the  $H\alpha$  emitters in each region as a function of SFR (top), specific SFR (middle), and stellar mass (bottom).

(A color version of this figure is available in the online journal.)

**Table 3**  
The Integrated Stellar Masses and SFRs of HAEs and DRGs

Region	Stellar Mass ( $\Sigma M_*$ ) [ $M_\odot$ ]			SFR ( $\Sigma$ SFR) [ $M_\odot \text{ yr}^{-1}$ ]	Specific SFR ( $\Sigma$ SFR / $\Sigma M_*$ ) [ $\text{yr}^{-1}$ ]
	HAE (blue)	HAE (red)	DRG	HAE	HAE+DRG
Clump 1	$1.3 \times 10^{11}$	$2.3 \times 10^{11}$	$1.2 \times 10^{12}$	$1.8 \times 10^3$	$1.4 \times 10^{-9}$
Clump 2	$3.9 \times 10^{11}$	$2.7 \times 10^{11}$	$1.2 \times 10^{12}$	$3.4 \times 10^3$	$2.2 \times 10^{-9}$
Clump 3	$8.2 \times 10^{10}$	$9.1 \times 10^{10}$	$1.1 \times 10^{11}$	$1.0 \times 10^3$	$5.4 \times 10^{-9}$
All clumps	$6.1 \times 10^{11}$	$6.0 \times 10^{11}$	$2.2 \times 10^{12}$	$6.2 \times 10^3$	$2.2 \times 10^{-9}$
Others	$4.1 \times 10^{11}$	$1.8 \times 10^{11}$	$9.2 \times 10^{11}$	$3.2 \times 10^3$	$2.4 \times 10^{-9}$
Entire field	$1.0 \times 10^{12}$	$7.8 \times 10^{11}$	$2.8 \times 10^{12}$	$9.4 \times 10^3$	$2.4 \times 10^{-9}$

**Notes.** The numbers are also divided into clumps and the other region. For HAEs, blue and red ones are separated at  $J - K_s = 1.38$  (same as the DRG criterion). For DRGs, the field contamination from foreground/background fields along the line of sight is statistically subtracted using the general field data (MODS). In estimation of specific SFR for combined samples with HAE and DRG, stellar masses are calculated by summing up those for HAE (blue) and DRG. The radio galaxy in clump-1 is excluded in this table because its  $H\alpha$  flux is severely contaminated by the AGN component.

On the other hand, as another possibility, the red HAEs can be quiescent galaxies with AGN activity in the galaxy core, rather than dusty starburst galaxies. Even in that case, the fact that the red HAEs are clustered in the high density region is very interesting. This is because the considered situation suggests that AGN activity is enhanced in the core regions of the clumps; thus, AGNs must significantly influence the evolution of high- $z$  galaxies in the high density region. Perhaps AGN activity has something to do with the process of quenching the star formation of cluster galaxies, i.e., the so-called AGN feedback. Although it is difficult to determine which of the hypotheses are true between dust starbursts and quiescent galaxies hosting an AGN with only the data now available, in any case, there is no doubt that galaxies are activated in the densest regions such as clumps at  $z \sim 2.5$ .

In lower- $z$  clusters ( $z \lesssim 1.0$ ), the fraction of star-forming galaxies to all cluster members decreases moving closer to

cluster centers or as the number density of galaxies increases (e.g., Kodama et al. 2004; Koyama et al. 2010, 2011). In this USS 1558-003 proto-cluster, however, it is difficult to completely sample red quiescent galaxies since DRGs have broad redshift distribution such as  $2 \lesssim z \lesssim 4$  and also contain both populations of quiescent galaxies and dusty starbursts. This makes it hard for us to quantify the fraction of star-forming galaxies in this proto-cluster. However, even if we assume that all the DRGs are quiescent galaxies associated with the proto-cluster at  $z = 2.53$ , a large fraction of proto-cluster members are star formers, and there are far fewer red quiescent galaxies.

## 5.2. Extended $H\alpha$ Emission in Radio Galaxy

As shown in Figure 6, the radio galaxy USS 1558-003 has quite an extended  $H\alpha$  emission with an apparent scale of  $\sim 4''.5$  or a physical scale of  $\sim 36$  kpc. Although the spatially

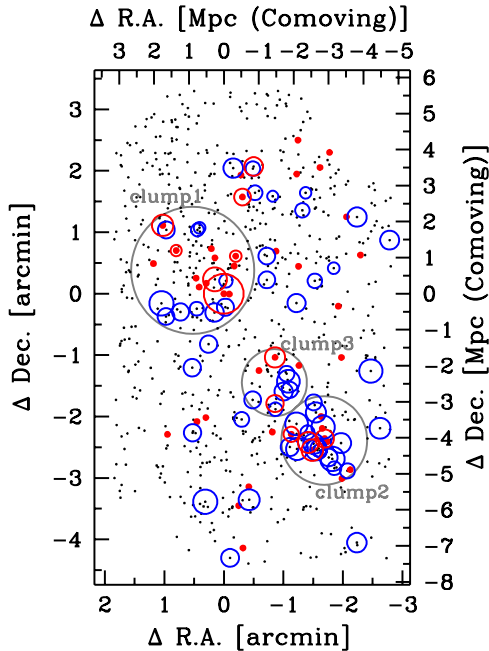


**Figure 11.** Similar to Figure 5, but the size of the circles is now scaled with SFR, in the sense that larger symbols show higher SFRs of the  $H\alpha$  emitters. The red  $H\alpha$  emitters with  $J - K_s > 1.38$  (DRGs criterion) are also specified with red circles. The red filled dots show DRGs.

(A color version of this figure is available in the online journal.)

extended nebular line emissions ( $Ly\alpha$  and  $H\alpha$ ) have already been recognized around this radio galaxy (Villar-Martín et al. 2007; Humphrey et al. 2008), we here reveal for the first time the two-dimensional distribution of  $H\alpha$  emission. Such extended nebular emission is a remarkable feature commonly seen in HzRGs (e.g., Heckman et al. 1991; Humphrey et al. 2007). In particular, it is well known that they show extended  $Ly\alpha$  emission aligned with radio structure (alignment effect). Our extended  $H\alpha$  emission is tilted with a position angle (P.A.) of  $50^\circ$  (Figure 6). This direction is approximately aligned to but slightly different from the radio axis which has the P.A. of  $75^\circ$  (Pentericci et al. 2000). Based on the integral field spectroscopy, Villar-Martín et al. (2007) found that the extent of the  $Ly\alpha$  emission is  $\sim 9''.0 \times 7''.5$  and is misaligned by  $\sim 30^\circ \pm 5^\circ$  relative to the radio structures. Therefore, the direction of the stretch of the  $H\alpha$  emission is more or less similar to that of  $Ly\alpha$  emission. However, the size of the  $H\alpha$  emission is  $\sim 4''.5 \times 3''.0$ , which is much smaller than the  $Ly\alpha$  emission. It is possible that this smaller size of  $H\alpha$  emission is due to the fact that the surface brightness of the outer region is less than the detection limit. To check the possibility, we compare the distribution of  $Ly\alpha$  flux density given in Villar-Martín et al. (2007) with the NB2315- $K_s$  image and find that the  $H\alpha$  emission can be detected at more than  $2\sigma$  if the  $Ly\alpha/H\alpha$  ratio is constant over the whole region where the  $Ly\alpha$  emission is detected. This means the ratio of  $Ly\alpha/H\alpha$  is not constant but is larger in the outer region of the radio galaxy. Such a smaller size of  $H\alpha$  emission compared to  $Ly\alpha$  emission is also seen in the radio galaxy MRC 1138-262 at  $z = 2.16$  (Kurk et al. 2002). Kurk et al. (2002) concluded that such fairly extended  $Ly\alpha$  emission is due to scattered radiation. Since we see a similar nature in the USS 1558-003 radio galaxy, the existence of abundant scattering material around the radio galaxy trapped in deep potential wells and large  $Ly\alpha$  emission probably due to resonant scattering seem to be common characteristics of HzRGs.

Furthermore, we find that the radio galaxy also has extended emission in the  $B$  and  $r'$  band, where there seems to be a contribution of  $Ly\alpha$  and  $HeII$  emissions to some extent in the  $B$  and  $r'$  band, respectively. However, we do not see any extended emission in the  $K_s$  band. Such extended emission in the rest-frame UV wavelengths and the compactness of the old stellar component may suggest that star-forming activity is also currently ongoing in the extended regions. In that case, such extended star formation is likely triggered by some physical processes associated with the radio activity. The jet-induced star formation is one plausible option (e.g., Bicknell et al. 2000; Hatch et al. 2011).

Many studies have been conducted to investigate the physical origin of nebular emission around the radio galaxy. Possible mechanisms include the photoionization by AGNs, young stars, and X-ray emission from shock heated gas, and collisional ionization by jet-induced shock (e.g., Miley & De Breuck 2008 and references therein). Although the ionization mechanism is not yet completely understood, recent studies suggest that AGNs could be the dominant source to ionize the surrounding nebular gas (e.g., Humphrey et al. 2008; Miley & De Breuck 2008). However, for radio galaxies at  $z \sim 1$ , Best et al. (2000) found that the cause of nebular emission is dependent on the size of radio morphology based on the diagnostic with line ratios of nebular emission. Small sources with a radio structure smaller than  $\lesssim 150$  kpc tend to have emission originated from shock ionization, while larger sources prefer the mechanism of photoionization by AGNs. Since the radio observation of USS 1558-003 shows that the size of the radio galaxy is  $9''.2$  (74 kpc; Pentericci et al. 2000), the shock ionization would be preferred. It is therefore interesting to investigate the origin of  $H\alpha$  emission of this radio galaxy in greater detail.

For this purpose, a diagnostic with nebular emission in rest-frame optical wavelength is useful. Humphrey et al. (2008) conducted optical and NIR spectroscopies in which a slit was placed on the radio galaxy along the radio axis and investigated the ratios of detected emission lines. They detected many emission lines in the rest-frame wavelength range of  $\lambda = 1216\text{--}6585 \text{ \AA}$  and found that the radio galaxy has a broad  $H\alpha$  emission line with a velocity width of  $12,000 \text{ km s}^{-1}$ , and that the amount of dust is negligibly small ( $A_v \sim 0$ ). Consequently, they concluded that the line ratios were best explained by AGN photoionization. However, they also found that the sources with high  $A_v$  do not show evidence for jet-gas interactions, while the sources undergoing strong jet-gas interactions have low  $A_v$ . The small amount of dust in this radio galaxy implies that the surrounding gas is undergoing interaction with the jet-induced shock. If this is indeed the case, the result is consistent with the proposed relation between the ionization mechanism and the radio size. It is suggested, therefore, that the shock induced star formation is occurring to some extent as well as AGN photoionization; thus, both mechanisms are probably contributing to the large extent of the  $H\alpha$  emission. It is difficult, however, to quantify the relative contribution of the two mechanisms, and it is beyond the scope of this paper. Integral field spectroscopy at NIR is essential to resolving the two-dimensional structure of the emission line regions and to fully understanding the physical origins of nebular emission.

## 6. CONCLUSIONS

We have conducted a panoramic narrow-band imaging of HAEs in the proto-cluster candidate around the radio galaxy USS 1558-003 at  $z = 2.53$  using the NB2315 filter

( $\lambda_c = 2.313 \mu\text{m}$ ,  $\Delta\lambda = 0.027 \mu\text{m}$ ) installed in MOIRCS on the Subaru Telescope. This target is known as an overdense region where DRGs are clustered (Kodama et al. 2007). We have confirmed that this is indeed a rich proto-cluster in the making, with lots of star-forming galaxies (HAEs) associated with the radio galaxy. We have mapped out the two-dimensional structure of the proto-cluster and investigated the star-forming activities and the stellar mass content of this forming cluster. The main results we have found are summarized below.

1. The proto-cluster is mainly composed of three conspicuous groups of galaxies. One of these surrounds the radio galaxy, the second is about 1.5 Mpc (physical scale) away from the radio galaxy to the southwest, and the third is between the two clumps. These groups show significant excess in the number densities of both HAEs and DRGs. Their close separations suggest that they would merge together in the near future and grow to a single, more massive galaxy cluster at a later time.
2. A large fraction of the HAEs in this proto-cluster have SFRs higher than  $100 M_\odot \text{ yr}^{-1}$ , indicating that at  $z \sim 2.5$ , the progenitors of cluster early-type galaxies are vigorously forming in the biased high density regions. Star formation activity is high everywhere irrespective of environment within the proto-cluster region, and the properties of individual HAEs show little environmental dependence, except that the HAEs in the densest clump may have slightly higher SFRs compared to those in other regions.
3. Most of the HAEs have blue colors, but some emitters have very red colors comparable to DRG (i.e.,  $J - K_s > 1.38$ ). Those red emitters are located on the fainter side of the red sequence on the color–magnitude diagram, except for the radio galaxy itself. Moreover, the red HAEs tend to be clustered in the three highest density clumps in contrast to lower- $z$  clusters, where similar red emitters are avoiding the cluster cores and preferentially located in the medium density regions or the outskirts of the clusters. Since the red emitters are likely to be dusty starburst galaxies in the transitional phase, this result may indicate that some environmental effects, such as galaxy–galaxy interaction, are at work on galaxies in the dense proto-cluster core at  $z = 2.53$ , and they are just changing their properties rapidly.
4. The radio galaxy shows a large  $\text{H}\alpha$  halo extended over  $\sim 4''5$  (i.e., 36 kpc), indicating that some ionization mechanisms (AGNs, young stars, and shocks) are at work in the material surrounding the radio galaxy. Such a spatial extent of  $\text{H}\alpha$  emission is still much smaller than the  $\text{Ly}\alpha$  halo. This means that the  $\text{Ly}\alpha$  emission is severely extended by resonant scattering.

The results we present in this paper are all intriguing, and there is no doubt that proto-clusters at  $z > 2$  have high star-forming activity and are in a vigorously evolving phase. However, we need to investigate more samples of proto-clusters at  $z > 2$  in detail in order to answer the question of whether our results represent the universal properties of proto-clusters at  $z > 2$  or show the specific characteristics of the USS1558 proto-cluster. Our ongoing MAHALO-Subaru project has been surveying other proto-clusters as well as unbiasedly selected fields at similar redshifts, enabling us to reveal the universality or variation of properties among proto-clusters at  $z > 2$ . Such discussion will be presented in our future papers (e.g., Koyama et al. 2012).

We thank the anonymous referee for carefully reading our manuscript and giving useful comments. All of the data used in this paper were collected at the Subaru Telescope, which is operated by the National Astronomical Observatory of Japan. We thank the Subaru Telescope staff for their invaluable help in assisting our observations with Suprime-Cam and MOIRCS. We acknowledge Dr. Philip Best for useful a discussion. M.H. is grateful for the financial support from the Japan Society for the Promotion of Science (JSPS) fund, “Institutional Program for Young Researcher Overseas Visits” to stay at the IfA, the Royal Observatory of Edinburgh for two months.

*Facility:* Subaru

## REFERENCES

- Bertin, E., & Arnouts, S. 1996, *A&AS*, **117**, 393  
 Best, P. N., Röttgering, H. J. A., & Longair, M. S. 2000, *MNRAS*, **311**, 23  
 Bicknell, G. V., Sutherland, R. S., van Breugel, W. J. M., et al. 2000, *ApJ*, **540**, 678  
 Brammer, G. B., van Dokkum, P. G., & Coppi, P. 2008, *ApJ*, **686**, 1503  
 Bruzual, G., & Charlot, S. 2003, *MNRAS*, **344**, 1000  
 Butcher, H., & Oemler, A., Jr. 1978, *ApJ*, **219**, 18  
 Butcher, H., & Oemler, A., Jr. 1984, *ApJ*, **285**, 426  
 Byrd, G., & Valtonen, M. 1990, *ApJ*, **350**, 89  
 Calzetti, D., Armus, L., Bohlin, R. C., et al. 2000, *ApJ*, **533**, 682  
 Cardelli, J. A., Clayton, G. C., & Mathis, J. S. 1989, *ApJ*, **345**, 245  
 Coleman, G. D., Wu, C., & Weedman, D. W. 1980, *ApJS*, **43**, 393  
 Cooper, M. C., Newman, J. A., Weiner, B. J., et al. 2008, *MNRAS*, **383**, 1058  
 Cucciati, O., Iovino, A., Marinoni, C., et al. 2006, *A&A*, **458**, 39  
 Daddi, E., Cimatti, A., Renzini, A., et al. 2004, *ApJ*, **617**, 746  
 Daddi, E., Dickinson, M., Morrison, G., et al. 2007, *ApJ*, **670**, 156  
 Doherty, M., Tanaka, M., De Breuck, C., et al. 2010, *A&A*, **509**, A83  
 Dressler, A., Oemler, A., Jr., Couch, W. J., et al. 1997, *ApJ*, **490**, 577  
 Fassbender, R., Nastasi, A., Bhringer, H., et al. 2011, *A&A*, **527**, L10  
 Franx, M., Labbé, I., Rudnick, G., et al. 2003, *ApJ*, **587**, L79  
 Garn, T., Sobral, D., Best, P. N., et al. 2010, *MNRAS*, **402**, 2017  
 Geach, J. E., Smail, I., Best, P. N., et al. 2008, *MNRAS*, **388**, 1473  
 Geach, J. E., Smail, I., Ellis, R. S., et al. 2006, *ApJ*, **649**, 661  
 Giavalisco, M., Ferguson, H. C., Koekemoer, A. M., et al. 2004, *ApJ*, **600**, L93  
 Gobat, R., Daddi, E., Onodera, M., et al. 2011, *A&A*, **526**, A133  
 Gunn, J. E., & Gott, J. R., III. 1972, *ApJ*, **176**, 1  
 Gunn, J. E., & Stryker, L. L. 1983, *ApJS*, **52**, 121  
 Hatch, N. A., Kurk, J. D., Pentericci, L., et al. 2011, *MNRAS*, **415**, 2993  
 Hatch, N. A., Overzier, R. A., Kurk, J. D., et al. 2009, *MNRAS*, **395**, 114  
 Hayashi, M., Kodama, T., Koyama, Y., Tadaki, K.-i., & Tanaka, I. 2011, *MNRAS*, **415**, 2670  
 Hayashi, M., Kodama, T., Koyama, Y., et al. 2010, *MNRAS*, **402**, 1980  
 Heckman, T. M., Miley, G. K., Lehnert, M. D., & van Breugel, W. 1991, *ApJ*, **370**, 78  
 Hilton, M., Lloyd-Davies, E., Stanford, S. A., et al. 2010, *ApJ*, **718**, 133  
 Hopkins, A. M., & Beacom, J. F. 2006, *ApJ*, **651**, 142  
 Humphrey, A., Villar-Martín, M., Fosbury, R., et al. 2007, *MNRAS*, **375**, 705  
 Humphrey, A., Villar-Martín, M., Vernet, J., et al. 2008, *MNRAS*, **383**, 11  
 Ichikawa, T., Suzuki, R., Tokoku, C., et al. 2006, *Proc. SPIE*, **6269**, 626916  
 Kajisawa, M., Ichikawa, T., Tanaka, I., et al. 2011, *PASJ*, **63**, 379  
 Kajisawa, M., Kodama, T., Tanaka, I., Yamada, T., & Bower, R. 2006a, *MNRAS*, **371**, 577  
 Kajisawa, M., Konishi, M., Suzuki, R., et al. 2006b, *PASJ*, **58**, 951  
 Kauffmann, G., White, S. D. M., Heckman, T. M., et al. 2004, *MNRAS*, **353**, 713  
 Kennicutt, R. C., Jr. 1998, *ARA&A*, **36**, 189  
 Kodama, T., Arimoto, N., Barger, A. J., & Aragón-Salamanca, A. 1998, *A&A*, **334**, 99  
 Kodama, T., Balogh, M. L., Smail, I., Bower, R. G., & Nakata, F. 2004, *MNRAS*, **354**, 1103  
 Kodama, T., Bell, E. F., & Bower, R. G. 1999, *MNRAS*, **302**, 152  
 Kodama, T., Tanaka, I., Kajisawa, M., et al. 2007, *MNRAS*, **377**, 1717  
 Kong, X., Daddi, E., Arimoto, N., et al. 2006, *ApJ*, **638**, 72  
 Koyama, Y., Kodama, T., Nakata, F., Shimasaku, K., & Okamura, S. 2011, *ApJ*, **734**, 66  
 Koyama, Y., Kodama, T., Shimasaku, K., et al. 2008, *MNRAS*, **391**, 1758  
 Koyama, Y., Kodama, T., Shimasaku, K., et al. 2010, *MNRAS*, **403**, 1611  
 Koyama, Y., Kodama, T., Tadaki, K., et al. 2012, *MNRAS*, submitted

- Kriek, M., van der Wel, A., van Dokkum, P. G., Franx, M., & Illingworth, G. D. 2008, *ApJ*, **682**, 896
- Kron, R. G. 1980, *ApJS*, **43**, 305
- Kuiper, E., Hatch, N. A., Röttgering, H. J. A., et al. 2010, *MNRAS*, **405**, 969
- Kuiper, E., Hatch, N. A., Venemans, B. P., et al. 2011, *MNRAS*, **417**, 1088
- Kurk, J. D., Pentericci, L., Overzier, R. A., Röttgering, H. J. A., & Miley, G. K. 2004a, *A&A*, **428**, 817
- Kurk, J. D., Pentericci, L., Röttgering, H. J. A., & Miley, G. K. 2002, *RevMexAA Conf. Ser.*, **13**, 191
- Kurk, J. D., Pentericci, L., Röttgering, H. J. A., & Miley, G. K. 2004b, *A&A*, **428**, 793
- Ly, C., Malkan, M. A., Kashikawa, N., et al. 2007, *ApJ*, **657**, 738
- Madau, P. 1995, *ApJ*, **441**, 18
- Madau, P., Ferguson, H. C., Dickinson, M. E., et al. 1996, *MNRAS*, **283**, 1388
- McLure, R. J., Kukula, M. J., Dunlop, J. S., et al. 1999, *MNRAS*, **308**, 377
- Miley, G., & De Breuck, C. 2008, *A&AR*, **15**, 67
- Miley, G. K., Overzier, R. A., Tsvetanov, Z. I., et al. 2004, *Nature*, **427**, 47
- Miyazaki, S., Komiyama, Y., Sekiguchi, M., et al. 2002, *PASJ*, **54**, 833
- Moore, B., Katz, N., Lake, G., Dressler, A., & Oemler, A. 1996, *Nature*, **379**, 613
- Ouchi, M., Shimasaku, K., Akiyama, M., et al. 2005, *ApJ*, **620**, L1
- Ouchi, M., Shimasaku, K., Okamura, S., et al. 2004, *ApJ*, **611**, 660
- Papovich, C., Momcheva, I., Willmer, C. N. A., et al. 2010, *ApJ*, **716**, 1503
- Pentericci, L., Röttgering, H. J. A., Miley, G. K., Carilli, C. L., & McCarthy, P. 1997, *A&A*, **326**, 580
- Pentericci, L., Van Reeve, W., Carilli, C. L., Röttgering, H. J. A., & Miley, G. K. 2000, *A&AS*, **145**, 121
- Rocca-Volmerange, B., Le Borgne, D., De Breuck, C., Fioc, M., & Moy, E. 2004, *A&A*, **415**, 931
- Rodighiero, G., Daddi, E., Baronchelli, I., et al. 2011, *ApJ*, **739**, L40
- Salpeter, E. E. 1955, *ApJ*, **121**, 161
- Schlegel, D. J., Finkbeiner, D. P., & Davis, M. 1998, *ApJ*, **500**, 525
- Seymour, N., Stern, D., De Breuck, C., et al. 2007, *ApJS*, **171**, 353
- Sobral, D., Best, P. N., Matsuda, Y., et al. 2012, *MNRAS*, **420**, 1926
- Steidel, C. C., Adelberger, K. L., Dickinson, M., et al. 1998, *ApJ*, **492**, 428
- Suzuki, R., Tokoku, C., Ichikawa, T., et al. 2008, *PASJ*, **60**, 1347
- Tadaki, K.-I., Kodama, T., Koyama, Y., et al. 2011, *PASJ*, **63**, 437
- Tanaka, I., Breuck, C. D., Kurk, J. D., et al. 2011, *PASJ*, **63**, 415
- Tanaka, M., Kodama, T., Arimoto, N., et al. 2005, *MNRAS*, **362**, 268
- Tran, K., Papovich, C., Saintonge, A., et al. 2010, *ApJ*, **719**, L126
- Ueda, Y., Akiyama, M., Ohta, K., & Miyaji, T. 2003, *ApJ*, **598**, 886
- Venemans, B. P., Röttgering, H. J. A., Miley, G. K., et al. 2005, *A&A*, **431**, 793
- Venemans, B. P., Röttgering, H. J. A., Miley, G. K., et al. 2007, *A&A*, **461**, 823
- Villar-Martín, M., Sánchez, S. F., Humphrey, A., et al. 2007, *MNRAS*, **378**, 416